

Charge–density analysis of an iron–sulfur protein at an ultra–high resolution of 0.48 Å

Yu Hirano^{1*†}, Kazuki Takeda^{1*} & Kunio Miki¹

The fine structures of proteins, such as the positions of hydrogen atoms, distributions of valence electrons and orientations of bound waters, are critical factors for determining the dynamic and chemical properties of proteins. Such information cannot be obtained by conventional protein X-ray analyses at 3.0–1.5 Å resolution, in which amino acids are fitted into atomically unresolved electron-density maps and refinement calculations are performed under strong restraints^{1,2}. Therefore, we usually supplement the information on hydrogen atoms and valence electrons in proteins with pre-existing common knowledge obtained by chemistry in small molecules. However, even now, computational calculation of such information with quantum chemistry also tends to be difficult, especially for polynuclear metalloproteins³. Here we report a charge-density analysis of the high-potential iron–sulfur protein from the thermophilic purple bacterium *Thermochromatium tepidum* using X-ray data at an ultra-high resolution of 0.48 Å. Residual electron densities in the conventional refinement are assigned as valence electrons in the multipolar refinement. Iron 3d and sulfur 3p electron densities of the Fe₄S₄ cluster are visualized around the atoms. Such information provides the most detailed view of the valence electrons of the metal complex in the protein. The asymmetry of the iron–sulfur cluster and the protein environment suggests the structural basis of charge storing on electron transfer. Our charge-density analysis reveals many fine features around the metal complex for the first time, and will enable further theoretical and experimental studies of metalloproteins.

Fine structural information, including the positions of hydrogen atoms and distributions of valence electrons, is essential for understanding the full properties of protein molecules; in particular, of electron transfer metalloproteins in photosynthesis and respiration. However, it is difficult to obtain such information with theoretical and experimental analyses. Therefore, experimental visualization of valence electrons and hydrogen atoms is of great value in elucidating the molecular mechanisms of protein functions. We have previously performed crystallographic investigations of photosynthetic proteins from *T. tepidum*^{4–6}. The high-potential iron–sulfur protein (HiPIP) is critical for electron transfer in bacterial photosynthesis. HiPIP from *T. tepidum* consists of 83 residues and possesses one Fe₄S₄ cluster at the centre of the protein. The protein gives high-quality crystals suitable for X-ray crystallographic analysis at ultra-high resolution⁷. It has been reported that the redox properties of the Fe₄S₄ cluster are attributable to interactions between the cluster and surrounding ligands, both in Fe₄S₄ and iron–sulfur proteins^{8,9} as well as in analogue compounds¹⁰. Therefore, we performed an experimental charge-density analysis of HiPIP in its reduced state. This is the first case, to our knowledge, of charge-density analysis being applied to metalloproteins, although it has been used previously for several proteins^{11–14}.

A diffraction data set at 0.48 Å resolution was collected using high-energy synchrotron X-rays ($\lambda = 0.45$ Å) (Extended Data Table 1

and Extended Data Fig. 1). This is equivalent to one of the highest-resolution data sets in the Protein Data Bank (<http://www.rcsb.org/pdb/home/home.do>), and it allowed us to perform structure refinement using the conventional independent spherical atom model (ISAM) without geometric restraints. Even after ISAM refinement, however, many residual electron densities were observed around each atom (Extended Data Fig. 2). Peaks of residual electron density were on the covalent bonds and around the carbonyl oxygen atoms of peptide bonds (Extended Data Fig. 2a), as well as on the covalent bonds of aromatic rings (Extended Data Fig. 2b). In the Fe₄S₄ cluster, peaks were symmetrically distributed around the Fe atoms (Extended Data Fig. 2c). The charge-density information of the electron densities was analysed with a multipolar atom model (MAM)¹⁵. The *R* factor was reduced from 8.24% (*R*_{free} = 8.63%) to 7.16% (*R*_{free} = 7.80%) by applying the charge-density analysis. The final structure contained hydrogen atoms of all 83 residues. In addition, 42 hydrogen atoms of water molecules were also included (Extended Data Table 1). The deformation map¹⁵ reveals the distribution of valence electrons in the protein. The fine structural information both of hydrogen atoms and of valence electrons highlights detailed views of intra-molecular interactions in the protein.

The dihedral angle ω of C _{α} –C–N'–C _{α} ' in a peptide bond, where prime symbols represent the atoms in the next residue, defines the planarity of the peptide bond, and the planar *trans* peptide shows an angle ω of 180°. Although some non-planar peptide bonds have been observed in protein crystal structures determined at ultra-high resolutions¹⁶, a planar geometry is adopted in the protein structure at ordinary resolutions¹⁷. In HiPIP, the peptides deviating approximately 10° or more from the planar ω angle are mainly located around the cysteine residues that are covalently bound to the Fe atoms of the Fe₄S₄ cluster (Fig. 1A). The distortion of peptide bonds is also observed in the positions of amide hydrogen atoms (Fig. 1B). Almost all hydrogen atoms deviating from the C–N'–C _{α} ' plane are in the non-planar peptide bonds (Extended Data Table 2). These hydrogen atoms are concentrated in the proximal region of the Fe₄S₄ cluster. The deviation of hydrogen atoms is plausibly influenced by the hydrogen bonds they form, in which the donor hydrogen atoms are pointed towards the lone pair electron density of the acceptor atoms (Fig. 1B). The same features have also been observed for the donor hydrogen atoms in the crystal structures of small molecules¹⁸. Three (Cys43, Cys61 and Cys75) out of four cysteine residues have distorted peptide bonds, while Cys46 does not (Extended Data Table 2). NMR data suggest that σ -type delocalization of Fe orbitals occurs through Fe–(Cys–S _{γ}) bonds¹⁹. This may further affect distortion of the peptide bonds. Indeed, Cys46 has the longest Fe–(Cys–S _{γ}) bond (Extended Data Table 3). The non-planarity causes partial breakdown of the resonance of the peptide bonds^{20,21}.

Non-spherical distribution of electron density is clearly observed around the atoms of Fe₄S₄(Cys–S _{γ})₄ (Fig. 2a). Lobes of electron density

¹Department of Chemistry, Graduate School of Science, Kyoto University, Sakyo-ku, Kyoto 606-8502, Japan. †Present address: Quantum Beam Science Research Directorate, National Institutes for Quantum and Radiological Science and Technology, Tokai-mura, Ibaraki 319-1195, Japan.

*These authors contributed equally to this work.

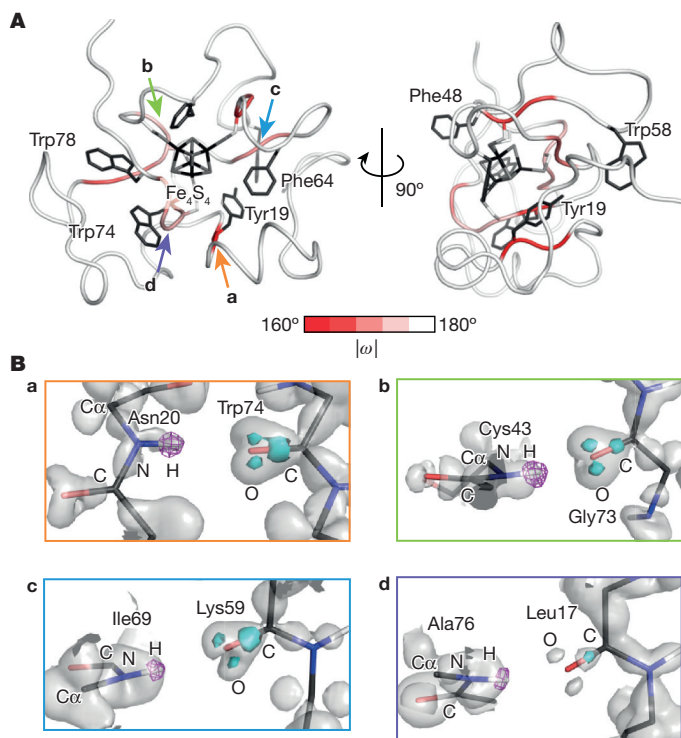


Figure 1 | Crystal structure of HiPIP at 0.48 Å resolution. **A**, Overall structure of HiPIP. Non-hydrogen atoms of aromatic side-chains, non-hydrogen atoms of cysteine residues and atoms of the Fe₄S₄ cluster are depicted as stick models. The main-chain atoms are shown as a tube model and single conformational residues are coloured according to the omega angles ($|\omega|$) from 160° (red) to 180° (white). The main-chain atoms of multi-conformational residues are coloured white. The aromatic side-chains are coloured dark grey. The Fe and S atoms of Fe₄S₄(Cys-S _{γ})₄ are coloured black and light grey, respectively. The orange, green, light blue and violet arrows represent the peptide bonds indicated in **B**. **B**, Hydrogen atoms in the peptide bonds of (a) Asn20, (b) Cys43, (c) Ile69 and (d) Ala76. The static deformation maps are shown as grey and cyan surfaces contoured at the levels of +0.1 and +0.3 electrons per cubic ångström, respectively. The omit maps of amide hydrogens are shown as a pink mesh contoured at the 3.0 σ level.

are symmetrically distributed around the Fe atoms, and correspond to the distribution of the Fe 3*d*-orbital electrons. The shapes of these electron-density lobes are quite similar among the four Fe atoms. In contrast to the Fe atoms, the bridging S and Cys-S _{γ} atoms are surrounded by more diffuse electron density that corresponds to the distribution of the S 3*p*-orbital electrons. The deformation electron densities of the individual S atoms do not exhibit any apparent similarity, unlike in the case of the Fe atoms. In some Fe–S bonds, the Fe 3*d* electron density points towards the S 3*p* electron density (Fig. 2b, c). Similar interactions in the valence density have been reported for the Ni–N bond in a transition metal complex²². However, the 3*d*–3*p* overlaps are smaller for bonds with shorter Fe–S bonds such as FE1–S2, while they are larger for longer bonds such as FE1–S3, in general.

The charge-density analysis presents the atomic charges of Fe₄S₄(Cys-S _{γ})₄ in HiPIP (Fig. 2d and Extended Data Table 4). The total atomic charge of Fe₄S₄(Cys-S _{γ})₄ is –1.5. This value is close to the total of the formal charges of Fe₄S₄(Cys-S _{γ})₄ in the reduced state. The atomic charge of FE1 (+0.9) is lower than those of FE2 (+1.2), FE3 (+1.1) and FE4 (+1.5). The atomic charge of S4 (–1.6) is significantly lower than those of other bridging S atoms (from –0.5 to –0.4). The atomic charges of Cys43-S _{γ} (–1.5) and Cys75-S _{γ} (–1.3) are lower than those of Cys46-S _{γ} (–0.1) and Cys61-S _{γ} (–0.3). The FE1 atom is coordinated by the ligand sulfur atoms, with the sum of the charges (–4.1) being more negative than for the other three Fe atoms (–2.7 to –2.6).

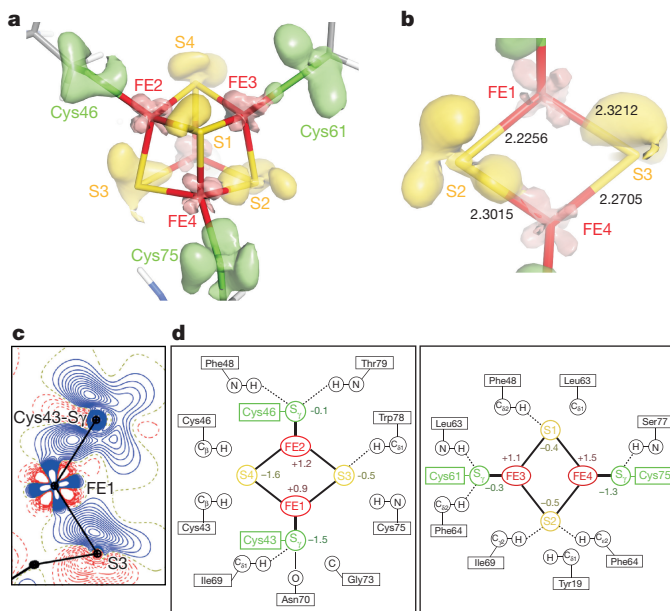


Figure 2 | The Fe₄S₄ cluster. **a**, The three-dimensional representation of the static deformation map of Fe₄S₄(Cys-S _{γ})₄. The orientation of the cluster is the same as the left panel of Fig. 1A. The isosurface represents the electron density contoured at the level of +0.2 electrons per cubic ångström. **b**, A close-up view for the plane of FE1–S3–FE4–S2. Bond lengths are indicated in the figure. **c**, The static deformation maps of the plane consisting of FE1, S3 and Cys43-S _{γ} atoms. The contour interval is 0.05 electrons per cubic ångström. Blue solid, red dashed and yellow dashed lines denote positive, negative and zero contours, respectively. **d**, Schematic representation of Fe₄S₄(Cys-S _{γ})₄. Left, the plane of FE1–S4–FE2–S3; right, the plane of FE3–S1–FE4–S2. The atomic charges for each atom are indicated. The dashed lines indicate interactions between valence densities of sulfur atoms and hydrogen atoms, and the thin lines indicate interactions between valence densities of sulfur atoms and non-hydrogen atoms.

On the basis of the Atoms in Molecules (AIM) theory²³, the bond topological properties can be derived from the charge-density analysis²⁴. The Laplacian and gradient maps display bond paths as well as boundaries of the respective atoms. The crossing point of the bond path and the boundary between two atoms is defined as the bond critical point (BCP). Distortions of the bond paths were clearly observed in the Fe–S bonds of Fe₄S₄(Cys-S _{γ})₄ (Fig. 3a, b). The BCPs exist between all Fe–S bonds (Extended Data Table 5). The electron density at the BCP (ρ_{BCP}) values for most Fe–S bonds have a negative correlation with bond lengths, as expected^{24,25}. However, those for FE1–S2 and FE2–S1 do not follow this rule (Fig. 3c). These two bonds have low ρ_{BCP} values despite short bond lengths. This fact is consistent with weak 3*d*–3*p* overlaps as shown in the deformation map (Fig. 2). The bond strengths are unequal among the four Fe–S bonds of each Fe atom. The Fe–(Cys-S _{γ}) bonds give the highest ρ_{BCP} values (Extended Data Table 5). In addition, the BCPs are located at closer positions to Fe atoms than the other three Fe–S bonds. This feature of Fe–(Cys-S _{γ}) may give some contribution to the distortion of the Fe₄S₄ cluster from the *T_d* symmetry, in addition to the spin coupling scheme²⁶ and the difference in bond length²⁷. Cys46, which is the only cysteine residue showing the planer peptide bond, gives the lowest ρ_{BCP} among the four Fe–(Cys-S _{γ}) bonds (Extended Data Table 5). This may be further evidence for the weaker interaction between FE2 and Cys46 as stated above. The Laplacian of electron densities ($\nabla^2\rho$) at all BCPs in Fe₄S₄(Cys-S _{γ})₄ is positive, as in the case of other transition metal complexes²².

The contributions of valence electrons in the interactions between Fe₄S₄(Cys-S _{γ})₄ and the protein environment are clearly visualized in the charge-density analysis (Fig. 2d). Valence electrons of Cys-S _{γ} atoms

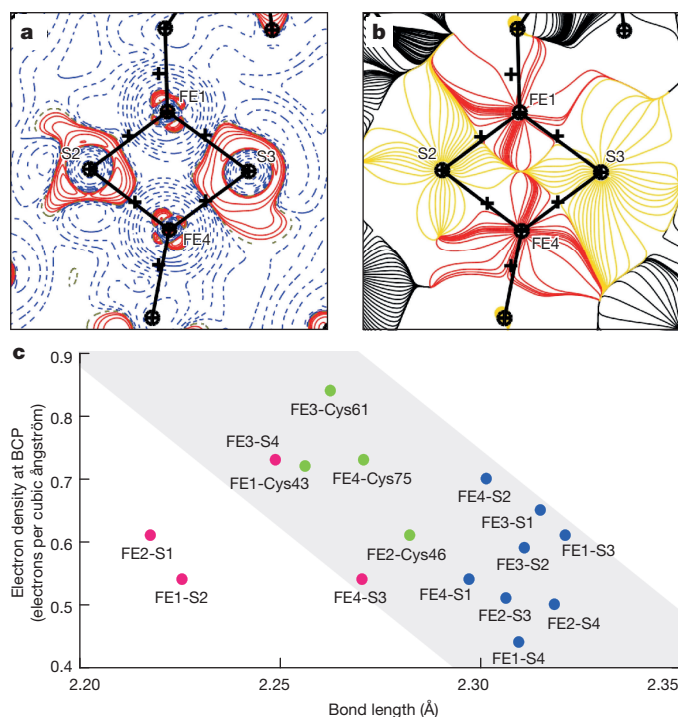


Figure 3 | Topological analysis of charge density in the Fe_4S_4 cluster. **a**, The Laplacian $\nabla^2\rho$ map in the plane of $FE1-S_3-Fe_4-S_2$. Contour interval is 0.05 electrons per ångström to the fifth power. Red solid lines represent negative values and blue dashed lines represent positive values. BCPs are shown as crosses. **b**, The gradient vector fields in the same plane as in **a**. **c**, Relationship between bond length and ρ_{BCP} . Filled circles in blue, pink and green are for intra-subcluster $Fe-S$, inter-subcluster $Fe-S$ and $Fe-(Cys-S_\gamma)$, respectively.

of Cys43, Cys46, Cys61 and Cys75 interact with the carbonyl oxygen atom of Asn70 and H atom of Ile69- $C_{\delta 1}$ (Extended Data Fig. 3a), the main-chain amides of Phe48 and Thr79 (Fig. 4a), the main-chain amide of Leu63 and the H atom of Phe64- $C_{\delta 2}$ (Extended Data Fig. 3b), and the main-chain amide of Ser77 (Extended Data Fig. 3c), respectively. Valence electrons of S_1 , S_2 and S_3 interact with the H atom of Phe48- $C_{\delta 2}$ (Extended Data Fig. 3d), the H atoms of Phe64- $C_{\alpha 2}$ and Ile69- $C_{\gamma 2}$ (Extended Data Fig. 3e), and the H atom of Trp78- $C_{\delta 1}$ (Fig. 4b). No interactions are observed between S_2 and the H atom of Tyr19- $C_{\delta 1}$ (Extended Data Fig. 3e), and S_3 and the main-chain amide of Cys75 (Fig. 4b), although these are in close proximity. The S_4 atom does not interact with the H atoms of Cys43- C_β and Cys46- C_β (Extended Data Fig. 3f). In addition, the S_4 atom is not surrounded by aromatic side chains. The interaction between valence electrons and H atoms has correlation with atomic charges of S atoms. S_4 with the largest atomic charge (-1.6) has no such interactions, while other bridging S atoms with smaller charges (-0.5 to -0.4) have (Fig. 2d). Furthermore, this rule is consistent for Cys-S atoms. Cys46- S_γ and Cys61- S_γ with smaller charges (-0.1 and -0.3) have two interactions, while Cys43- S_γ and Cys75- S_γ with larger charges (-1.5 and -1.3) have only one interaction. Charge transfer from S to H atoms through the interactions may be involved in the reduction of the negative charges of S. Taken together with atomic charges and topological properties, detailed views of interactions between the cluster and surrounding ligands imply that the $FE1$ atom together with $FE2$, S_4 and Cys43- S_γ atoms are crucial for storing electronic charges in the reduced HiPIP. The atomic charges in this paper were derived from the AIM analysis. It has been shown that the AIM analysis provides the most reliable estimation of the electronic properties for model clusters²⁶. In our study, the absolute values of the AIM charges are generally larger than charges derived from the multipolar parameters (Extended Data Table 4). This can be attributed

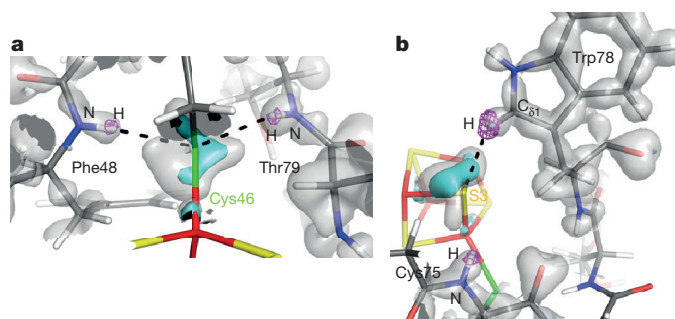


Figure 4 | Interaction network around the Fe_4S_4 cluster. **a**, Deformation electron density around the Cys46- S_γ atom. The main-chain amides of Phe48 and Thr79 are located close to the Cys46- S_γ atom. The static deformation maps are shown as grey and cyan surfaces contoured at the levels of $+0.1$ and $+0.3$ electrons per cubic ångström, respectively, and the omit map of hydrogen atoms is shown as a pink mesh contoured at the 3.0σ level. The dashed lines indicate interactions between valence densities of sulfur atoms and hydrogen atoms. **b**, Deformation electron density around S_3 of the Fe_4S_4 cluster. The main-chain amide of Cys75 and the H atom of Trp78- $C_{\delta 1}$ are located close to the S_3 atom.

to charge transfer from S to Fe atoms. However, it is difficult to discuss this only from our results.

The cuboid $[Fe_4S_4]^{2+}$ cluster is divided into two rhombic $[Fe_2S_2]^{+}$ subclusters²⁷. Each subcluster has ferromagnetically coupled two Fe atoms with d^9 configuration ($S = 9/2$). The two subclusters are anti-ferromagnetically coupled to each other to give $S = 0$. In HiPIP from *T. tepidum*, one subcluster consists of $FE1$, $FE2$, S_3 and S_4 atoms and coordinates Cys43 and Cys46, while another subcluster consists of $FE3$, $FE4$, S_1 and S_2 atoms and coordinates Cys61 and Cys75 by taking the results of HiPIP from *Chromatium vinosum*^{27,28} into consideration. The assignment is consistent with the overlap manner in the Fe-S bonds and the topological analysis in which $FE1-S_2$ and $FE2-S_1$ between two subclusters show a distinctive feature. It was suggested that the redox reaction is localized in one of the two subclusters²⁷. This is likely to be consistent with our implication for electron-storing atoms.

The charge-density analysis of this study experimentally reveals a subatomic structure of respective atoms in the polynuclear metal cluster in the HiPIP. This result, in combination with spectroscopic and computational data, will contribute to the understanding of the relationship between structure and function of metalloproteins.

Online Content Methods, along with any additional Extended Data display items and Source Data, are available in the online version of the paper; references unique to these sections appear only in the online paper.

Received 2 October 2015; accepted 12 April 2016.

Published online 18 May 2016.

- Hendrickson, W. A. Stereochemically restrained refinement of macromolecular structures. *Methods Enzymol.* **115**, 252–270 (1985).
- Wlodawer, A., Minor, W., Dauter, Z. & Jaskolski, M. Protein crystallography for aspiring crystallographers or how to avoid pitfalls and traps in macromolecular structure determination. *FEBS J.* **280**, 5705–5736 (2013).
- Rokob, T. A., Srncic, M. & Rulíšek, L. Theoretical calculations of physico-chemical and spectroscopic properties of bioinorganic systems: current limits and perspectives. *Dalton Trans.* **41**, 5754–5768 (2012).
- Nogi, T., Fathir, I., Kobayashi, M., Nozawa, T. & Miki, K. Crystal structures of photosynthetic reaction center and high-potential iron-sulfur protein from *Thermochromatium tepidum*: thermostability and electron transfer. *Proc. Natl Acad. Sci. USA* **97**, 13561–13566 (2000).
- Liu, L., Nogi, T., Kobayashi, M., Nozawa, T. & Miki, K. Ultrahigh-resolution structure of high-potential iron-sulfur protein from *Thermochromatium tepidum*. *Acta Crystallogr. D* **58**, 1085–1091 (2002).
- Niwa, S. *et al.* Structure of the LH1-RC complex from *Thermochromatium tepidum* at 3.0 Å. *Nature* **508**, 228–232 (2014).
- Takeda, K., Kusumoto, K., Hirano, Y. & Miki, K. Detailed assessment of X-ray induced structural perturbation in a crystalline state protein. *J. Struct. Biol.* **169**, 135–144 (2010).
- Niu, S. & Ichiye, T. Insight into environmental effects on bonding and redox properties of $[4Fe-4S]$ clusters in proteins. *J. Am. Chem. Soc.* **131**, 5724–5725 (2009).

9. Glaser, T. *et al.* Protein effects on the electronic structure of the $[\text{Fe}_4\text{S}_4]^{2+}$ cluster in ferredoxin and HiPIP. *J. Am. Chem. Soc.* **123**, 4859–4860 (2001).
10. Dey, A. *et al.* Solvent tuning of electrochemical potentials in the active sites of HiPIP versus ferredoxin. *Science* **318**, 1464–1468 (2007).
11. Jelsch, C. *et al.* Accurate protein crystallography at ultra-high resolution: valence electron distribution in crambin. *Proc. Natl Acad. Sci. USA* **97**, 3171–3176 (2000).
12. Schmidt, A., Jelsch, C., Ostergaard, P., Rypniewski, W. & Lamzin, V. S. Trypsin revisited: crystallography at (sub) atomic resolution and quantum chemistry revealing details of catalysis. *J. Biol. Chem.* **278**, 43357–43362 (2003).
13. Fournier, B. *et al.* Charge density and electrostatic interactions of fidarestat, an inhibitor of human aldose reductase. *J. Am. Chem. Soc.* **131**, 10929–10941 (2009).
14. Zarychta, B. *et al.* Cholesterol oxidase: ultrahigh-resolution crystal structure and multipolar atom model-based analysis. *Acta Crystallogr. D* **71**, 954–968 (2015).
15. Hansen, N. K. & Coppens, P. Testing aspherical atom refinements on small-molecule data sets. *Acta Crystallogr. A* **34**, 909–921 (1978).
16. Berkholz, D. S., Driggers, C. M., Shapovalov, M. V., Dunbrack, R. L., Jr & Karplus, P. A. Nonplanar peptide bonds in proteins are common and conserved but not biased toward active sites. *Proc. Natl Acad. Sci. USA* **109**, 449–453 (2012).
17. Engh, R. A. & Huber, R. Accurate bond and angle parameters for X-ray structure refinement. *Acta Crystallogr. A* **47**, 392–400 (1991).
18. Murray-Rust, P. & Glusker, J. P. Directional hydrogen bonding to sp^2 - and sp^3 - hybridized oxygen atoms and its relevance to ligand-macromolecule interactions. *J. Am. Chem. Soc.* **106**, 1018–1025 (1984).
19. Bertini, I., Donaire, A., Felli, I. C., Luchinat, C. & Rosato, A. ^1H and ^{13}C NMR studies of an oxidized HiPIP. *Inorg. Chem.* **36**, 4798–4803 (1997).
20. Improta, R., Vitagliano, L. & Esposito, L. Peptide bond distortions from planarity: new insights from quantum mechanical calculations and peptide/protein crystal structures. *PLoS ONE* **6**, e24533 (2011).
21. Wang, Y.-F., Yu, Z.-Y., Wu, J. & Liu, C.-B. Electron delocalization and charge transfer in polypeptide chains. *J. Phys. Chem. A* **113**, 10521–10526 (2009).
22. Smith, G. T. *et al.* Experimental determination of the electron density topology in a non-centrosymmetric transition metal complex: $[\text{Ni}(\text{H}_3\text{L})][\text{NO}_3][\text{PF}_6]$ [$\text{H}_3\text{L} = N,N',N''$ -tris(2-hydroxy-3-methylbutyl)-1,4,7-triazacyclononane]. *J. Am. Chem. Soc.* **119**, 5028–5034 (1997).
23. Bader, R. F. W. *Atoms in Molecules: A Quantum Theory* (Oxford Univ. Press, 1990).
24. Koritsanszky, T. S. & Coppens, P. Chemical applications of X-ray charge-density analysis. *Chem. Rev.* **101**, 1583–1628 (2001).
25. Gibbs, G. V. *et al.* Theoretical electron density distributions for Fe- and Cu-sulfide earth materials: a connection between bond length, bond critical point properties, local energy densities, and bonded interactions. *J. Phys. Chem. B* **111**, 1923–1931 (2007).
26. Harris, T. V. & Szilagy, R. K. Iron-sulfur bond covalency from electronic structure calculations for classical iron-sulfur clusters. *J. Comput. Chem.* **35**, 540–552 (2014).
27. Dey, A. *et al.* Sulfur K-edge XAS and DFT calculations on $[\text{Fe}_4\text{S}_4]^{2+}$ clusters: effects of H-bonding and structural distortion on covalency and spin topology. *Inorg. Chem.* **44**, 8349–8354 (2005).
28. Mouesca, J. M., Noodleman, L., Case, D. A. & Lamotte, B. Spin densities and spin coupling in iron-sulfur clusters: a new analysis of hyperfine coupling constants. *Inorg. Chem.* **34**, 4347–4359 (1995).

Acknowledgements We thank K. Kusumoto and H. Ohno for their contributions in the initial steps of the work, and T. Tsujinaka and S. Niwa for their contributions in the preparation of the manuscript. We also thank the BL41XU beamline staff of SPring-8 for their help in data collection. This work was supported by a Grant-in-Aid for Scientific Research (number 23657073 to K.T.) and the Photon and Quantum Basic Research Coordinated Development Program (to K.M.) from the Ministry of Education, Culture, Sports, Science and Technology of Japan.

Author Contributions K.M. initiated and supervised the project. K.T. designed the experiments. Y.H. prepared crystals. Y.H. and K.T. performed data collection and the crystallographic analysis. Y.H., K.T. and K.M. discussed the results. Y.H. wrote the initial draft, and K.T. and K.M. revised the manuscript.

Author Information The coordinates and structure factors have been deposited in the Protein Data Bank under accession number 5D8V. Reprints and permissions information is available at www.nature.com/reprints. The authors declare no competing financial interests. Readers are welcome to comment on the online version of the paper. Correspondence and requests for materials should be addressed to K.M. (miki@kuchem.kyoto-u.ac.jp).

METHODS

No statistical methods were used to predetermine sample size. The experiments were not randomized. The investigators were not blinded to allocation during experiments and outcome assessment.

X-ray diffraction experiment. Crystals of DTT-reduced HiPIP were prepared as previously described⁷. The X-ray wavelengths were set to 0.45 Å (27.6 keV) at the BL41XU beamline of SPring-8 (proposal numbers 2008B-1337, 2010A1237 and 2010B1284 to K.T.). The diffraction intensities were measured using a Rayonix MX-225 CCD detector. The crystals were cooled during the data collection at 100 K using a nitrogen-gas stream. Three data sets for reflections in ultra-high, medium- and low-resolution regions were separately collected for the different positions of a single crystal (0.8 mm × 0.2 mm × 0.1 mm), and the data sets for reflections in medium and low-resolution regions were collected with attenuated X-ray exposure. The data set for ultra-high resolution was collected using a helical data collection procedure²⁹ with a microbeam of 50 μm × 50 μm. The maximum dose in each irradiated position was limited to ~6 × 10⁵ Gy. The dose was estimated using the RADDOSE program³⁰. The diffraction data sets were integrated and scaled using the HKL2000 program package³¹. The relative *B* factors, *R*_{sym} and other crystallographic statistics, which represent the metrics for radiation damage, did not show significant changes during the data collection (Extended Data Fig. 1). Three data sets for ultra-high-, medium-, and low-resolution regions were merged into a complete data set.

Structure refinement with the ISAM. The test set for free *R* factor calculation was set to be the same as in the 0.7 Å-resolution data of HiPIP⁷ in the resolution range 20–0.7 Å and extended to 0.48 Å resolution by randomly selecting 5% of reflections. Structure refinement was started from the low-dose structure of the reduced form of HiPIP (Protein Data Bank accession number 3A39) using the SHELXL program³². Positional and anisotropic displacement parameters were refined for all non-hydrogen atoms. Restraints for bond lengths and angles were removed for non-hydrogen atoms of single conformational residues and for the Fe₄S₄ cluster. All of the hydrogen atoms of amino-acid residues were included in the model, and only the hydrogen atoms of water molecules which were observed in the *F*_o – *F*_c map contoured at the 2.0σ level were included. Bond lengths and angles involving hydrogen atoms were constrained using the riding model in the SHELXL program. The final structure in the SHELXL refinement contains 34 multiple-conformation residues and was refined to the *R*_{work} and *R*_{free} factors of 8.24% and 8.63%.

Charge-density analysis with the MAM. The charge-density analysis with the MAM was performed using the MoPro program³³. The refinement for HiPIP followed the procedure for human aldose reductase³⁴, but was slightly modified. The scale factors were refined in the whole resolution range 20–0.48 Å. Bulk solvent parameters with the scale factors were refined in the resolution range 20–1.0 Å. The subsequent refinement processes were performed for the non-hydrogen atoms of single conformational residues, the atoms in the Fe₄S₄ cluster and the oxygen atoms of water molecules with two hydrogen atoms (H₂O). Positional and anisotropic displacement parameters were refined in the whole resolution range. Then, positional and anisotropic displacement parameters were refined using only high-resolution reflections (high-order refinement). In the high-order refinement, resolution ranges used for refinement were sequentially changed as 1.0–0.48 Å, 0.9–0.48 Å, 0.8–0.48 Å, 0.7–0.48 Å and 0.65–0.48 Å. Positions of hydrogen atoms were changed to the standard geometry determined by neutron diffraction experiments of small molecules³⁵ and were fixed in the subsequent refinement steps. After the high-order refinement, strong peaks remained near the atom positions of the Fe₄S₄ cluster in the residual electron-density map. The short path lengths of low-resolution reflections cause an incomplete absorption of the high-energy X-rays in the CCD detector³⁶. To correct the resolution-dependence in the absorption of the CCD detector, we used an exponential function by which the observed structure factors were fitted to the calculated ones as $F_{\text{obs}}^{\text{corr}}(hkl) = F_{\text{obs}}(hkl)/EF$ where $EF = \sum_i a_i \exp[b_i(\sin\theta/\lambda - c_i)] + d$, and the coefficients of *a*_{*i*}, *b*_{*i*}, *c*_{*i*} (*i* = 1, 2, 3) and *d* were fitted to $\langle |F_{\text{obs}}|/|F_{\text{c}}| \rangle$ in 50 resolution bins by a least-squares method.

The MAM is expressed as shown in equation (1):

$$\rho_{\text{atom}}(\mathbf{r}) = \rho_{\text{core}}(r) + P_{\text{val}}\kappa^3\rho_{\text{val}}(\kappa r) + \sum_{l=0}^{l_{\text{max}}} \kappa'^3 R_{nl}(\kappa' r) \sum_{m=0}^l P_{lm\pm} y_{lm\pm}(\theta, \varphi) \quad (1)$$

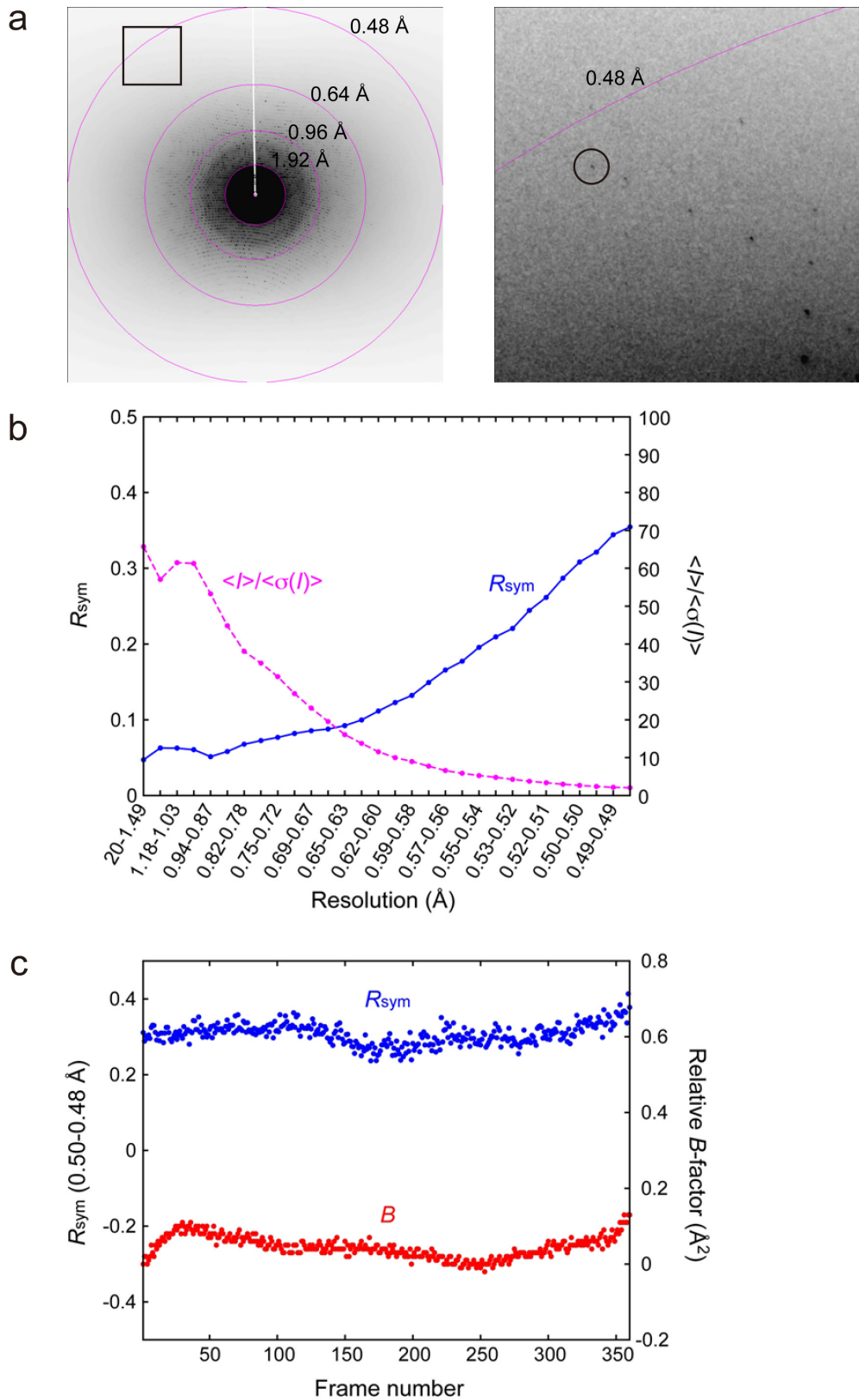
The ρ_{atom} , ρ_{core} and ρ_{val} represent the total, spherical core and spherical valence electron densities, and P_{val} and $P_{lm\pm}$ are the spherical valence and deformation multipole populations. R_{nl} is the Slater-type radial functions and $y_{lm\pm}$ the real spherical harmonics. The κ and κ' parameters are electron-density expansion/contraction coefficients. The parameters used for the least-squares refinement are P_{val} , $P_{lm\pm}$, κ and κ' . Multipolar parameters were transferred to all of the amino-acid residues and H₂O molecules from the experimental library multipolar atom model (ELMAM)³⁷. The multipolar parameters were assigned to the octupole

level ($l_{\text{max}} = 3$) for C, N and O atoms, the hexadecapole level ($l_{\text{max}} = 4$) for S and Fe atoms and the dipole level ($l_{\text{max}} = 1$) for H atoms. Solvent atoms other than H₂O were treated as spherical with a neural charge. The definition of local axes was derived from the multipolar library for the atoms of the amino-acid residues and H₂O. The local axes for the sulfur atoms of Fe₄S₄(Cys-S-)₄ were defined to coincide with the directions of the unit cell axes. The *d*-orbital populations for the local axes (*x*, *y*, *z*) were calculated and are listed in Extended Data Table 6. The local axes were set as shown in Extended Data Fig. 4, according to refs 38, 39.

Initial values of multipolar parameters for Fe₄S₄(Cys-S-)₄ were unavailable in ELMAM. However, the atomic charge of the Fe atom is difficult to define properly in the multipolar refinement because of the diffused distribution of the 4s electrons³⁸. In the multipolar refinement of HiPIP, the initial values of P_{val} and κ parameters were obtained from a grid search procedure for Fe, S and Cys-S- atoms. The κ' parameter was fixed to 1.00. All of the $P_{lm\pm}$ parameters ($l > 0$) were refined for the atoms of Fe₄S₄(Cys-S-)₄, but the monopole P_{00} parameters were fixed to zero because the P_{00} parameter has a high correlation with the P_{val} parameter. Finally, the initial values of P_{val} and κ parameters were determined to be 7.5 and 1.10 for Fe atoms, 6.5 and 0.99 for S atoms and 6.5 and 0.99 for Cys-S- atoms.

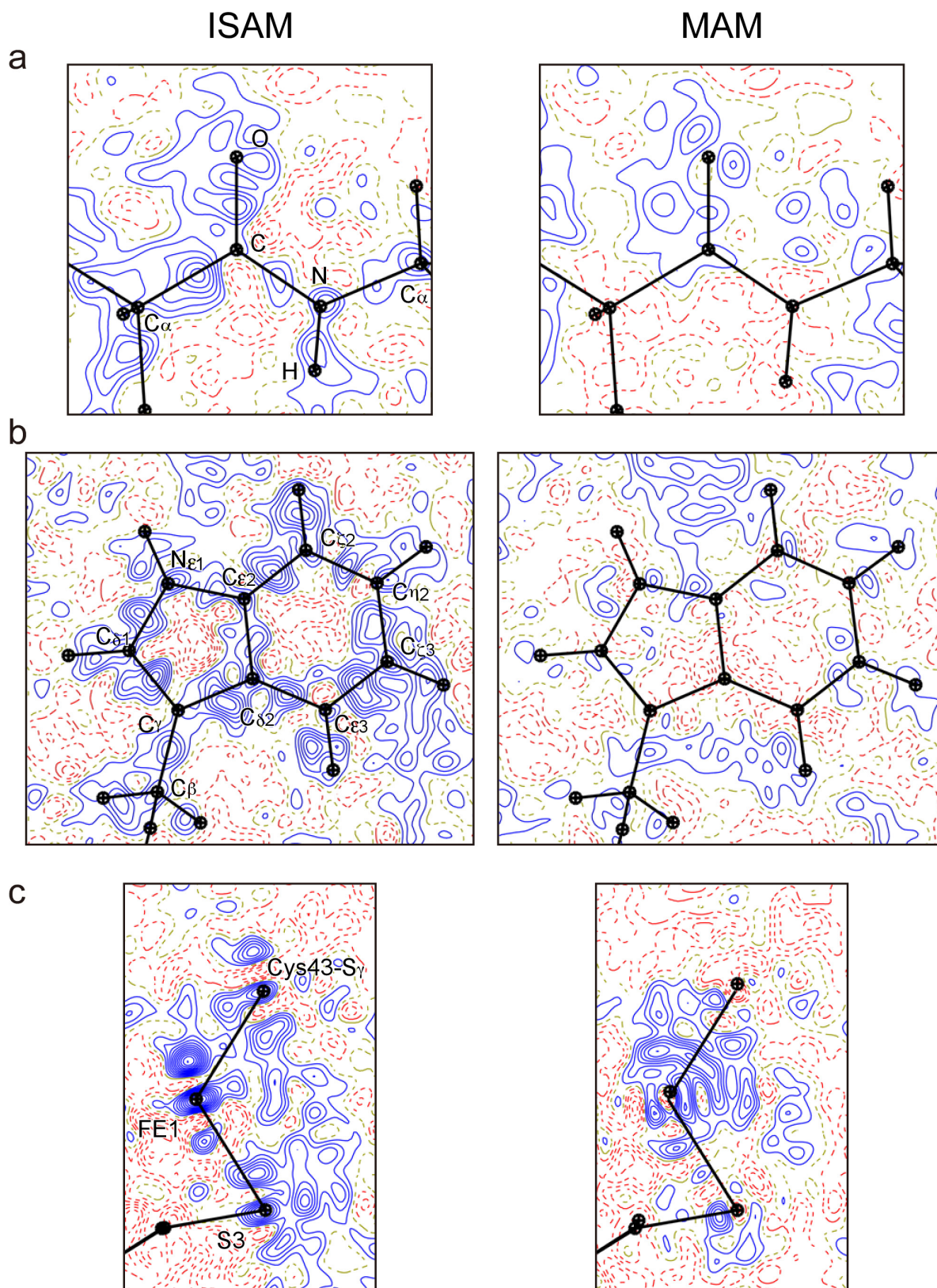
After the grid search, the $P_{lm\pm}$ parameters were refined for single conformational residues, Fe₄S₄(Cys-S-)₄ and H₂O molecules. Following the refinement of the $P_{lm\pm}$ parameters, positional and anisotropic displacement parameters were refined for the non-hydrogen atoms. In the refinement of the P_{val} parameters it was difficult to obtain reasonable values for the atomic charges in Fe₄S₄(Cys-S-)₄. Thus, the P_{val} parameters were refined after the $P_{lm\pm}$ parameters. The differences in the atomic scattering factors for Fe²⁺ and Fe³⁺ were prominent in the resolution range lower than 1.5 Å. Reasonable atomic charges were obtained in the refinement of P_{val} parameters with the resolution range 20–1.2 Å. The P_{val} parameters for single conformational residues were also refined, but the P_{val} parameters for hydrogen atoms were constrained to be the same as for the chemically equivalent atoms. The total number of electrons in the crystal was fixed during the refinement of P_{val} parameters. Finally, the *R*_{work} and *R*_{free} factors were converged to 7.16% and 7.80% (Extended Data Table 1). *B*_{eq} values for Fe₄S₄(Cys-S-)₄ in the final model are listed in Extended Data Table 4. The static deformation map in this paper was calculated by the equation $\Delta\rho_{\text{static}}(\mathbf{r}) = \sum_{j=1}^{N_{\text{at}}} [\rho_{\text{multi}}(\mathbf{r} - \mathbf{r}_j) - \rho_{\text{IAM}}(\mathbf{r} - \mathbf{r}_j)]$. The parameters ρ_{multi} and ρ_{IAM} represent the electron density calculated from the MAM and from the ISAM, respectively. The static deformation map is calculated excluding the contribution of the atomic displacement parameters of atoms. The two-dimensional contour maps were prepared using the VMOPro program and the three-dimensional figures were prepared using PyMOL⁴⁰. Topological analyses based on the AIM theory^{23,24} was performed with VMOPro. The atomic charges by the AIM theory were calculated with Bader⁴¹. The atomic charges by the equation of $q = N_{\text{val}} - P_{\text{val}}$, where N_{val} is the number of valence electrons in the neutral charge, were also calculated. The two methods gave highly correlated results as listed in Extended Data Table 4.

29. Flot, D. *et al.* The ID23-2 structural biology microfocus beamline at the ESRF. *J. Synchrotron Radiat.* **17**, 107–118 (2010).
30. Paithankar, K. S., Owen, R. L. & Garman, E. F. Absorbed dose calculations for macromolecular crystals: improvements to RADDOSE. *J. Synchrotron Radiat.* **16**, 152–162 (2009).
31. Otwinowski, Z. & Minor, W. Processing of X-ray diffraction data. *Methods Enzymol.* **276**, 307–326 (1997).
32. Sheldrick, G. M. A short history of SHELX. *Acta Crystallogr. A* **64**, 112–122 (2008).
33. Guillot, B., Viry, L., Guillot, R. & Lecomte, C. Refinement of proteins at subatomic resolution with MOPRO. *J. Appl. Cryst.* **34**, 214–223 (2001).
34. Guillot, B., Jelsch, C., Podjarny, A. & Lecomte, C. Charge-density analysis of a protein structure at subatomic resolution: the human aldose reductase case. *Acta Crystallogr. D* **64**, 567–588 (2008).
35. Allen, F. H. A systematic pairwise comparison of geometric parameters obtained by X-ray and neutron diffraction. *Acta Crystallogr. B* **42**, 515–522 (1986).
36. Wu, G., Rodrigues, B. L. & Coppens, P. The correction of reflection intensities for incomplete absorption of high-energy X-rays in the CCD phosphor. *J. Appl. Cryst.* **35**, 356–359 (2002).
37. Zarychta, B., Pichon-Pesme, V., Guillot, B., Lecomte, C. & Jelsch, C. On the application of an experimental multipolar pseudo-atom library for accurate refinement of small-molecule and protein crystal structures. *Acta Crystallogr. A* **63**, 108–125 (2007).
38. Holladay, A., Leung, P. & Coppens, P. Generalized relations between *d*-orbital occupancies of transition-metal atoms and electron-density multipole population parameters from X-ray diffraction data. *Acta Crystallogr. A* **39**, 377–387 (1983).
39. Sabino, J. R. & Coppens, P. On the choice of *d*-orbital coordinate system in charge-density studies of low-symmetry transition-metal complexes. *Acta Crystallogr. A* **59**, 127–131 (2003).
40. DeLano, W. L. The PyMol Molecular Graphics System (DeLano Scientific, 2002).
41. Yu, M. & Trinkle, D. R. Accurate and efficient algorithm for Bader charge integration. *J. Chem. Phys.* **134**, 064111 (2011).



Extended Data Figure 1 | Quality of the diffraction data at 0.48 Å resolution. **a**, The diffraction image. Right, zoom view of the boxed region at left. The resolution for each circle is indicated. **b**, R_{sym} (blue) and $\langle I \rangle / \langle \sigma(I) \rangle$ (pink) values are plotted for 30 resolution bins. **c**, Changes

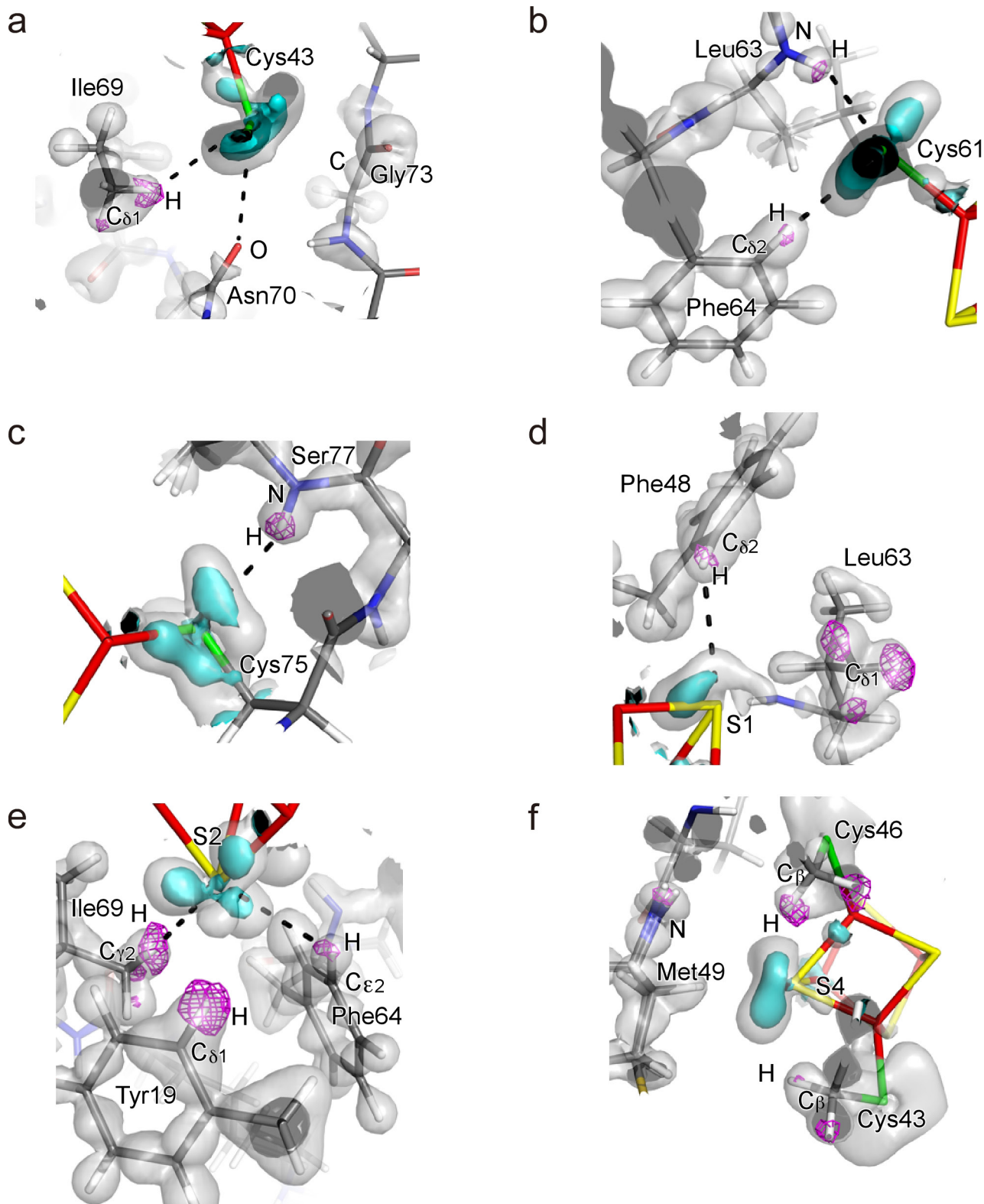
of R_{sym} at the highest-resolution shell (0.50–0.48 Å) and relative B factor in the course of the data collection. The R_{sym} (blue) and relative B factor (red) are plotted as functions of frame number.



Extended Data Figure 2 | Residual electron density for each refinement step. The left panels show the residual density after the ISAM refinement; the right panels show the residual density after the MAM refinement.

a, The plane of the peptide bond between Asn45 and Cys46. Maximum and minimum peaks are 0.33 and -0.22 electrons per cubic ångström for the ISAM analysis, and 0.18 and -0.20 electrons per cubic ångström for the MAM analysis. **b,** The plane of the aromatic ring of Trp74. Maximum and minimum peaks are 0.34 and -0.29 electrons per cubic ångström

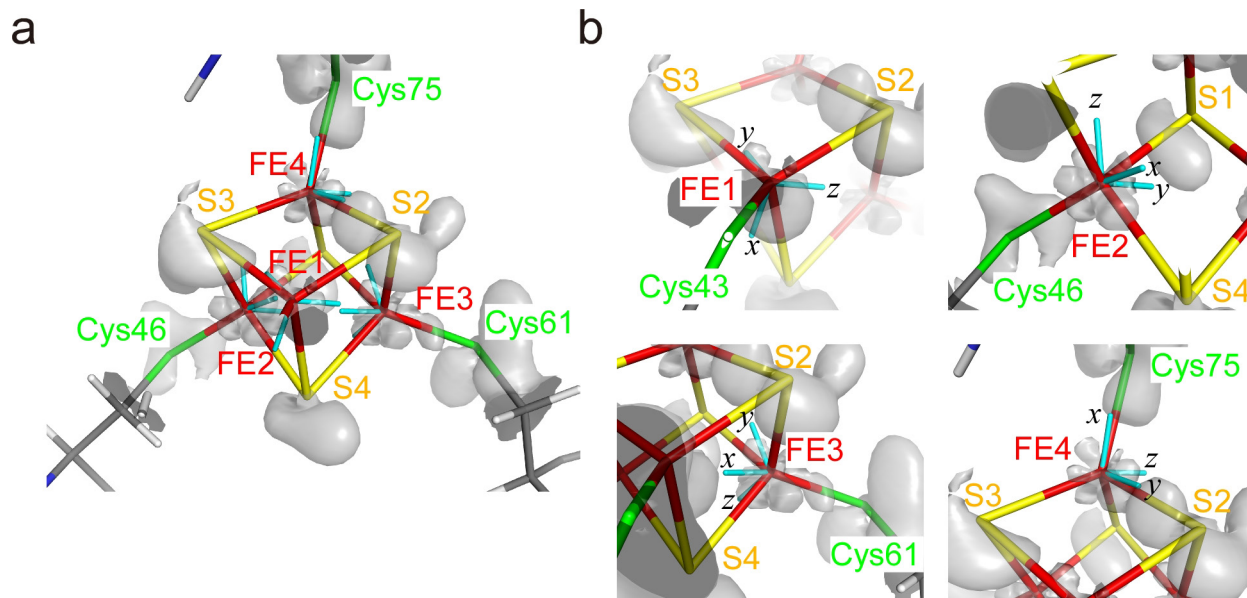
for the ISAM analysis, and 0.23 and -0.23 electrons per cubic ångström for the MAM analysis. **c,** The Fe_4S_4 cluster. The plane consists of FE1, S3 and Cys43-S γ atoms. Maximum and minimum peaks are 0.60 and -0.35 electrons per cubic ångström for the ISAM analysis, and 0.35 and -0.29 electrons per cubic ångström for the MAM analysis. The contour interval is 0.05 electrons per cubic ångström for all figures. Blue solid, red dashed and yellow dashed lines denote positive, negative and zero contours, respectively.



Extended Data Figure 3 | Interaction network around the Fe₄S₄ cluster.

a, Deformation electron density around the Cys43-S_γ atom. The main-chain oxygen atom of Asn70, the main-chain carboxyl carbon atom of Gly73 and the H atom of Ile69-C_{δ1} are located close to Cys43-S_γ. The static deformation maps are shown as grey and cyan surfaces contoured at the levels of +0.1 and +0.3 electrons per cubic ångström, respectively. The omit map of hydrogen atoms is shown as a pink mesh contoured at the 3.0σ level. The dashed lines indicate interactions between valence densities of sulfur atoms and hydrogen atoms. **b**, Deformation electron density around Cys61-S_γ. The main-chain amide of Leu63 and the H atom of

Phe64-C_{δ2} are located close to Cys61-S_γ. **c**, Deformation electron density around Cys75-S_γ. The main-chain amide of Ser77 is located close to Cys75-S_γ. **d**, Deformation electron density around S1 of the Fe₄S₄ cluster. The H atom of Phe48-C_{δ2} and the C_{δ1} atom of Leu63 are located close to S1. **e**, Deformation electron density around S2 of the Fe₄S₄ cluster. The H atoms of Tyr19-C_{δ1}, Phe64-C_{ε2} and Ile69-C_{γ2} are located close to S2. **f**, Deformation electron density around S4 of the Fe₄S₄ cluster. The H atom of Cys43-C_β, the H atom of Cys46-C_β and the amide nitrogen atom of Met49 are located close to S4.



Extended Data Figure 4 | The local axes for Fe atoms of $\text{Fe}_4\text{S}_4(\text{Cys-S-})_4$. **a**, Whole view of the local axes of the four Fe atoms. **b**, Close-up views of the local axes of each Fe atom (FE1–FE4). The static deformation maps of $\text{Fe}_4\text{S}_4(\text{Cys-S-})_4$ are represented as grey isosurfaces contoured at the level of +0.2 electrons per cubic ångström.

Extended Data Table 1 | Data collection and refinement statistics

HiPIP	
Data collection	
Space group	$P2_12_12_1$
Cell dimensions	
a, b, c (Å)	46.48, 58.91, 23.44
α, β, γ (°)	90, 90, 90
Resolution (Å)	20–0.48 (0.50–0.48)*
R_{sym} or R_{merge} (%)	5.6 (33.9)
$I/\sigma I$	61.1 (2.7)
Completeness (%)	96.3 (89.0)
Redundancy	5.4 (3.0)
Refinement	
Resolution (Å)	20–0.48
No. reflections	301,119
$R_{\text{work}}/R_{\text{free}}$ (%) (ISAM)	8.24/8.63
$R_{\text{work}}/R_{\text{free}}$ (%) (MAM)	7.16/7.80
No. non-H atoms	
Protein	848
Ligand/ion	72
Water	185
No. H atoms	
Protein	820
Ligand/ion	0
Water	42

*Highest-resolution shell is shown in parentheses.

Extended Data Table 2 | Dihedral and improper angles

	Dihedral angle (°)	Improper angle* (°)
Tyr19–Asn20	162.0	1.78
Asp22–Ala23	-177.0	0.98
Ala23–Thr24	177.0	1.01
Ala31–Ala32	176.4	1.20
Gln41–His42	168.3	0.01
His42–Cys43	-170.9	2.34
Cys43–Ala44	-175.2	2.52
Ala44–Asn45	-179.5	0.96
Gly60–Cys61	166.7	1.08
Leu68–Ile69	170.0	1.77
Gly73–Thr74	179.6	0.66
Thr74–Cys75	163.7	0.01
Cys75–Ala76	-172.8	2.18
Ala76–Ser77	170.7	1.10

*The improper angle is an angle between the C–N–C_α' and H'–N'–C_α' planes.

Extended Data Table 3 | Geometrical parameters in Fe₄S₄(Cys-S_γ)₄

Distance (Å)		Angle (°)	
FE1-S2	2.2256 (3)*	FE1-S2-FE4	73.12 (1)*
FE1-S4	2.3096 (4)	FE1-S2-FE3	73.53 (-)
FE1-S3	2.3212 (4)	FE1-S4-FE3	73.13 (1)
FE2-S1	2.2177 (3)	FE1-S4-FE2	72.81 (1)
FE2-S3	2.3064 (3)	FE1-S3-FE4	71.94 (1)
FE2-S4	2.3185 (4)	FE1-S3-FE2	72.81 (1)
FE3-S4	2.2489 (3)	FE2-S1-FE4	73.68 (-)
FE3-S2	2.3110 (4)	FE2-S1-FE3	73.14 (2)
FE3-S1	2.3150 (4)	FE2-S3-FE4	72.54 (2)
FE4-S3	2.2705 (3)	FE2-S4-FE3	72.51 (1)
FE4-S1	2.2972 (4)	FE3-S2-FE4	72.31 (1)
FE4-S2	2.3015 (4)	FE3-S1-FE4	72.31 (1)
FE1-FE2	2.7466 (3)	S1-FE2-S3	104.73 (2)
FE1-FE3	2.7161 (2)	S1-FE2-S4	105.32 (1)
FE1-FE4	2.6974 (3)	S1-FE4-S3	103.34 (1)
FE2-FE3	2.7018 (3)	S1-FE4-S2	106.39 (1)
FE2-FE4	2.7077 (3)	S1-FE3-S4	104.42 (1)
FE3-FE4	2.7212 (3)	S1-FE3-S2	105.49 (1)
FE1-(Cys43-S _γ)	2.2563 (3)	S2-FE1-S4	104.35 (2)
FE2-(Cys46-S _γ)	2.2824 (3)	S2-FE1-S3	105.51 (1)
FE3-(Cys61-S _γ)	2.2626 (4)	S2-FE4-S3	104.70 (1)
FE4-(Cys75-S _γ)	2.2709 (3)	S2-FE3-S4	103.56 (1)
(Tyr19-C _{δ1})-S2	3.673 (2)	S3-FE2-S4	105.06 (1)
(Phe48-N)-(Cys46-S _γ)	3.444 (1)	S3-FE1-S4	104.87 (1)
(Phe48-C _{δ2})-S1	3.792 (2)	(Cys43-S _γ)-FE1-S2	113.49 (1)
(Leu63-N)-(Cys61-S _γ)	3.375 (1)	(Cys43-S _γ)-FE1-S4	111.60 (2)
(Leu63-C _{δ1})-S1	3.525 (2)	(Cys43-S _γ)-FE1-S3	115.99 (2)
(Phe64-C _{δ2})-(Cys61-S _γ)	3.716 (2)	(Cys46-S _γ)-FE2-S1	114.63 (1)
(Phe64-C _{ε2})-S2	3.964 (2)	(Cys46-S _γ)-FE2-S3	115.38 (1)
(Ile69-C _{γ2})-S2	3.893 (2)	(Cys46-S _γ)-FE2-S4	110.79 (1)
(Asn70-O)-(Cys43-S _γ)	3.357 (1)	(Cys61-S _γ)-FE3-S4	117.52 (2)
(Cys75-N)-S3	3.401 (1)	(Cys61-S _γ)-FE3-S2	119.16 (2)
(Ser77-N)-(Cys75-S _γ)	3.365 (1)	(Cys61-S _γ)-FE3-S1	105.22 (2)
(Trp78-C _{δ1})-S3	3.771 (1)	(Cys75-S _γ)-FE4-S3	126.49 (2)
(Thr79-N)-(Cys46-S _γ)	3.526 (1)	(Cys75-S _γ)-FE4-S1	104.97 (2)
		(Cys75-S _γ)-FE4-S2	109.41 (1)

*Values in parentheses are estimated standard deviations given by full-matrix least-squares refinement.

Extended Data Table 4 | Atomic properties of $\text{Fe}_4\text{S}_4(\text{Cys-S}_\gamma)_4$

Atom	Charge (AIM)	Charge ($N-P_{\text{val}}$)	B_{eq} factor (\AA^2)
FE1	+0.92	+0.42 (12)*	2.32
FE2	+1.15	+0.58 (12)	2.31
FE3	+1.13	+0.97 (12)	2.40
FE4	+1.46	+1.33 (12)	2.33
S1	-0.39	-0.14 (27)	2.53
S2	-0.51	-0.36 (27)	2.47
S3	-0.52	-0.21 (28)	2.40
S4	-1.57	-1.40 (28)	2.46
Cys43-S $_\gamma$	-1.48	-1.38 (28)	2.51
Cys46-S $_\gamma$	-0.12	-0.16 (28)	2.36
Cys61-S $_\gamma$	-0.27	-0.20 (28)	2.82
Cys75-S $_\gamma$	-1.27	-1.11 (29)	2.44
Total	-1.47	-1.69	

*Values in parentheses are estimated standard deviations given by full-matrix least-squares refinement.

Extended Data Table 5 | Topological parameters at BCPs of Fe–S bonds

	d (Å)	d_1^* (Å)	ρ (e/Å ³)	$\nabla^2\rho$ (e/Å ⁵)
FE1-S2	2.2256	1.058	0.54	1.4
FE1-S3	2.3212	1.024	0.61	3.7
FE1-S4	2.3096	1.093	0.44	3.4
FE2-S1	2.2177	0.966	0.61	5.2
FE2-S3	2.3064	1.056	0.51	2.5
FE2-S4	2.3185	1.131	0.50	2.2
FE3-S1	2.3150	1.050	0.65	2.3
FE3-S2	2.3110	1.049	0.59	1.7
FE3-S4	2.2489	0.973	0.73	5.5
FE4-S1	2.2972	1.056	0.54	2.0
FE4-S2	2.3015	1.024	0.70	3.8
FE4-S3	2.2705	1.058	0.54	1.0
FE1-(Cys43-S _{γ})	2.2563	1.001	0.72	2.3
FE2-(Cys46-S _{γ})	2.2824	1.034	0.61	4.6
FE3-(Cys61-S _{γ})	2.2626	0.987	0.84	0.0
FE4-(Cys75-S _{γ})	2.2709	0.944	0.73	5.0

*Parameter d_1 is the distance between the Fe atom of the pair and the BCP.

Extended Data Table 6 | The *d*-orbital populations of iron atoms

	z^2	x^2-y^2	xz	yz	xy	total
FE1	2.00 (26.4%)	1.99 (26.3%)	0.98 (12.9%)	0.65 (8.6%)	1.97 (25.9%)	7.59
FE2	1.76 (23.7%)	1.93 (26.0%)	1.98 (26.7%)	0.83 (11.2%)	0.91 (12.3%)	7.43
FE3	1.99 (28.3%)	2.00 (28.4%)	1.01 (14.4%)	1.55 (22.0%)	0.49 (7.0%)	7.04
FE4	1.99 (29.9%)	1.05 (15.8%)	0.64 (9.7%)	0.99 (14.9%)	1.99 (29.9%)	6.68